Nanoscale Advances

ROYAL SOCIETY OF CHEMISTRY

PAPER

View Article Online
View Journal | View Issue

Cite this: *Nanoscale Adv.*, 2025, **7**, 6954

Enhanced thermoelectric performance, inter-layer coupling effects and reduced lattice thermal conductivity in two-dimensional transition metal oxides

Aadil Fayaz Wani,[a] Kulwinder Kaur,*[b] Baljinder Kaur,[a] Sikander Iqbal,[c] Shobhna Dhiman[a] and Shakeel Ahmad Khandy *[d]

Two-dimensional metal oxides exhibit excellent waste heat recovery response, but still their efficiency requires improvement for commercial viability. Herein, a computational simulation is used to investigate the inter-layer coupling effect in AA-stacked NiO_2, PdO_2 and PtO_2 bilayers and has provided evidence of their experimental feasibility by demonstrating negative binding energy and positive phonon modes. An approximately twofold increase in *ZT* of these bilayers is reported, compared to their monolayer counterparts. The first reason being narrowing of the electronic band gap (E_g = 1.18 eV, 1.57 eV, 1.79 eV) and a rise in electrical conductivity brought on by longer relaxation time of carriers, which contributes to the enhancement of power factor. Additionally, the presence of multiple minima/maxima of conduction/valence bands near the Fermi level simultaneously boosts electrical conductivity and the Seebeck coefficient. Second, the softening of phonon modes, which reduces phonon group velocity, and the presence of van der Waals interlayer interactions, collectively contribute to a notable decrease in lattice thermal conductivity. Moreover, high Grüneisen parameters of XO_2 bilayers significantly influence their lattice thermal conductivity. At 700 K, the lattice thermal conductivity (κ_l) drops to 8.69 W m^{-1} K^{-1}, 4.71 W m^{-1} K^{-1} and 1.93 W m^{-1} K^{-1}, respectively, for NiO_2, PdO_2 and PtO_2 bilayers, which is half of their monolayer counterparts. These effects collectively contribute to the improvement in *ZT* (1.05, 1.57, and 1.79, respectively). We anticipate that our observations will stimulate research on related low-dimensional materials for enhanced heat recovery performance.

Received 1st April 2025
Accepted 29th August 2025

DOI: 10.1039/d5na00303b

rsc.li/nanoscale-advances

Introduction

Green and renewable energy research in this era has been of much interest due of the depletion of natural resources and rising pollution levels on earth. Many forms of waste energy are emitted as heat, which negatively affects the current generation and, if it continues, will cause the earth to experience heat death.[1] This issue can be resolved to some degree by employing a solid-state thermoelectric device to recover the waste heat. This device operates on the Seebeck effect principle and allows for the control of an ever-increasing global temperature. Thermoelectric technology has been acknowledged as green energy technology; a dependable, economical, and pollution-free method of directly converting heat into electrical energy. A thermoelectric material produces a voltage between its two ends when waste heat creates a temperature difference between them.[2,3] The thermoelectric conversion efficiency of a thermoelectric material depends on a dimensionless parameter called figure of merit (*ZT*), which is a function of the Seebeck coefficient (*S*), electrical conductivity (σ) and total thermal conductivity (κ = electronic thermal conductivity (κ_e) + lattice thermal conductivity (κ_{ph})) given as:[4]

$$ZT = \frac{S^2 \sigma T}{k} \quad (1)$$

The value of *ZT* is limited by inter-twining of parameters involved in it. Researchers have developed many innovative approaches for improving thermoelectric performance of materials including electronic band structure modulation by inducing resonant states and band convergence. Additionally, manipulation of phonon transport using nano-structuring, defects, strain, and alloying diminishes lattice thermal conductivity.[5–7] Many commercially used high performance

[a]*Department of Physics, Punjab Engineering College (Deemed to be University), Chandigarh, India*

[b]*Mehr Chand Mahajan, DAV College for Women, Chandigarh, India. E-mail: kulwinderphysics@gmail.com*

[c]*ZJU-Hangzhou Global Scientific and Technological Innovation Center, Zhejiang University, 311200, China*

[d]*Frontier Research Institute for Interdisciplinary Sciences, Islamic University of Science & Technology, Awantipora, 192122, India. E-mail: shakeelkhandy11@gmail.com*

thermoelectric materials have been designed by adopting these methods, which provide high values of *ZT* even at room temperature.[8,9]

Dimensionality plays a very crucial role in electronic and phonon transport properties of a material.[10–15] The development of various synthesis techniques has made it possible to control the length scale of a material. Nano-materials such as quantum dots (0D), quantum wires (1D), nano-films (2D) and their combinations have been designed successfully in laboratories.[16,17] The thermoelectric performance of these quantum materials shows a positive response by increasing power factor while lowering lattice thermal conductivity.[18,19] Single layered two-dimensional (2D) materials, especially transition metal-based monolayers, show extraordinary thermoelectric behavior due to quantum confinement effects and large phonon scattering at surfaces.[20–24] Creating a quantum superlattice by stacking various layers together is an effective method for modifying the thermoelectric properties of single-layer materials.[25–27] In this approach, the in-plane bonding between constituent atoms is covalent, while the interactions between out-of-plane atoms are governed by van der Waals forces.[28] In bilayers, where two individual monolayers are held together by dispersion interactions, the electronic transport properties are nearly unaffected in the direction parallel to the plane while the weak interaction between adjacent layers leads to large scattering of phonons resulting in enhancement of *ZT*. A study conducted by A. Pandit *et al.* on the stability and thermoelectric properties of homo bilayer SnTe reveals an enhancement in the *ZT* value up to 4.61.[29] This improvement is approximately two times higher when compared to the *ZT* of SnTe monolayers. The primary factor contributing to this improvement is a significant decrease in lattice thermal conductivity.[30] A remarkably low lattice thermal conductivity of 0.90 is observed in SnSe bilayers when two layers of SnSe are stacked together with an interlayer spacing of 5.5 Å.[28] The *ZT* increases to 0.78, which is notably higher than its monolayer counterpart. Recent advances in thin-film deposition and oxide heterostructure engineering have opened up possibilities for fabricating ultrathin transition metal oxide layers.[31,32] Monolayer-like NiO_2 planes are already known to exist in layered cuprates and Ruddlesden–Popper-type structures, and can be stabilized using epitaxial techniques such as pulsed laser deposition (PLD) and molecular beam epitaxy (MBE).[32] Similarly, ultrathin PdO_2 and PtO_2 films have been experimentally realized in surface reconstructions and oxide thin-film growth, highlighting the viability of synthesizing such bilayer structures.[33–35] These developments, combined with the moderate interlayer binding energies calculated in our study, support the experimental feasibility of the proposed XO_2 bilayers for future thermoelectric applications.

Recent studies on the thermoelectric response of NiO_2, PdO_2 and PtO_2 monolayers have revealed remarkable thermoelectric behavior, characterized by high values of the Seebeck coefficient. These materials exhibit a *ZT* of 0.5, 0.6, and 0.7, respectively, which highlights their impressive thermoelectric performance.[36,37] However, it is worth noting that the high lattice thermal conductivity of these monolayers imposes limitations on their overall performance, indicating a need for modulation in this aspect to further enhance their thermoelectric efficiency. To investigate the impact of interlayer coupling on the transport and thermoelectric characteristics of 2D materials, our approach involves designing and examining three homo-bilayers XO_2 (X = Ni, Pd, Pt) based on their pristine monolayers. After confirming stability, a systematic study of thermoelectric transport properties is carried out using first principles calculations. Our findings provide a strategy for improving the performance of single layered thermoelectric materials and demonstrate their transport behavior and their applications and advantages in the realm of renewable energy.

Theoretical method

The present calculations are carried out under the framework of density functional theory as implemented in the Quantum Espresso package.[38] The generalized gradient approximation technique with the Perdew–Burke–Ernzerhof (PBE) functional and projector-augmented-wave (PAW) formalism were employed for exchange–correlation energy contributions and freezing of ion cores. All calculations are performed after confirming the convergence of different computational parameters. The energy cut-off for plane wave expansion and charge density is set to be 850 Ry and 80 Ry, respectively, and a $20 \times 20 \times 1$ *k*-point grid for Brillouin zone sampling is used for optimizing simulations.[39] The bilayer structures are fully relaxed until the energy differences are converged within 10^{-8} eV, with a Hellman–Feynman force convergence threshold of 10^{-5} eV Å^{-1}. The van der Waals interlayer interactions, which play a crucial role in deciding the properties of the bilayer, are included using VdW-D2 method of Grimme.[40] To avoid the fictitious interaction between periodic images, a vacuum region of 20 Å is employed perpendicular to the plane along the *z*-direction.

Semi-classical Boltzmann transport theory is used to compute the thermoelectric transport parameters based on the electronic band structure including the Seebeck coefficient (S), electrical conductivity (σ), and electronic thermal conductivity (κ_e). The theory is based on two approximations: rigid band approximation and approximation of constant relaxation-time.[41] Under these approximations, the electronic band structure is rigid during external doping and a fixed value of relaxation time is used for all temperatures.[42] All these calculations are performed with the help of the BoltzTrap program.[41] Additionally, a high dense *k*-mesh of $80 \times 80 \times 1$ is used for convergence of self-consistent calculations.

The ShengBTE code is utilized to compute the lattice thermal conductivities of XO_2 bilayers.[43] This involved solving the linear phonon Boltzmann transport equation (BTE) using the relaxation time approximation (RTA).[44,45] The precise interatomic force constants (IFCs) required are acquired by displacing few atoms simultaneously in the supercell, followed by calculating the forces acting on the remaining atoms. Harmonic IFCs were extracted using the Phonopy code,[46] while anharmonic IFCs were obtained through the Thirdorder Python tool integrated into the ShengBTE code. To calculate anharmonic IFCs, we utilized a $4 \times 4 \times 1$ supercell and considered interactions up to the 5th nearest neighbour with a cutoff radius of 8 Å. A *q*-mesh

of size 42 × 42 × 1 is chosen to sample the phonon wave-vector mesh in the ShengBTE calculations.

Results and discussion

Structural optimization and electronic band dispersion

Starting with structural optimization, by taking XO_2 (X = Ni, Pd, Pt) monolayers as fundamental constituents, we constructed different stacking configurations of bilayers like AA, AB and AA′ (AA + *na*, 0 < *n* < 1 and *a* is the lattice parameter) and explored their stabilities. Out of the three stacking arrangements considered, it was found that only the AA type of configuration exhibits chemical stability across all three bilayers, as evidenced by negative interlayer binding energy, which is calculated using the relation:[32]

$$E_b = (E_{(bilayer)} - 2E_{(monolayer)})/n \quad (2)$$

where $E_{(bilayer)}$ is the total energy of the XO_2 bilayer and $E_{(monolayer)}$ is the total energy of the isolated monolayer, and *n* is the total number of atoms in a unit cell of the bilayer. The binding energies are −115 meV per atom, −154 meV per atom and −306 meV per atom for NiO_2, PdO_2 and PtO_2 bilayers, respectively. These values suggest that there exist moderate interlayer (van der Waals (vdW)) interactions among the atoms in bilayers. Considering this geometrical configuration, all calculations are carried out exclusively with regard to this arrangement.

Pristine XO_2 monolayers stabilize in hexagonal structures, all with the same space group $P\bar{3}m1$.[36,37] The relaxed structure of XO_2 bilayers in AA stacking configuration is shown in Fig. 1. Owing to one X and two O atoms in the unit cell of single layered XO_2, their bilayer counterparts contain a total of six (two X and four O) atoms in the primitive unit cells. As we move down the group from Ni to Pt, the electronegativity of the transition metal atoms decreases. This reduction in electronegativity weakens the metal–oxygen bonding interactions, making the chemical bonds in NiO_2 stronger than those in PdO_2, which are in turn stronger than those in PtO_2. Consequently, the lattice parameters and bond lengths increase in the order: NiO_2 < PdO_2 < PtO_2, reflecting the weakening of bond strength. The same trend is observed in the interlayer spacing, which increases from NiO_2 to PtO_2 due to the reduced bonding affinity. Interestingly, this expansion in bond length and lattice constants leads to a decrease in bond angles, producing a reverse trend compared to bond length. The detailed structural parameters, including bond lengths, bond angles, and interlayer spacings, are summarized in Table 1. To further quantify the bond strength, we have calculated the harmonic force constants for the nearest-neighbour atom pairs. The results, presented in the SI (Fig. S1(d)), clearly show a decreasing trend in force constants from NiO_2 to PtO_2 consistent with the above analysis of structural parameters and phonon behaviour.

To infer electronic properties, which subsequently impact electrical conductivity and the Seebeck coefficient, we computed electronic band structures, along with projected and total density of states and the results are illustrated in Fig. 2. Except for the dispersion of bands close to the Fermi level and magnitude of the band-gap, the electronic band structures of XO_2 bilayers are extremely comparable to their monolayer

Table 1 Simulated values of lattice constants (*a*), bond lengths ($l_{(X-O)}$), bond angles ($\alpha_{(O-X-O)}$), interlayer spacings (*d*) and band-gaps (E_g) of XO_2 bilayers

					E_g (eV)	
Material	*a* (Å)	$l_{(Ni-O)}$ (Å)	$\alpha_{(O-X-O)}$	*d* (Å)	DFT	DFT + *U*
NiO_2	2.90	1.91	81.60°	3.99	0.89	1.18
PdO_2	3.11	2.09	80.64	4.01	1.06	1.53
PtO_2	3.17	2.13	78.80	4.03	1.43	1.79

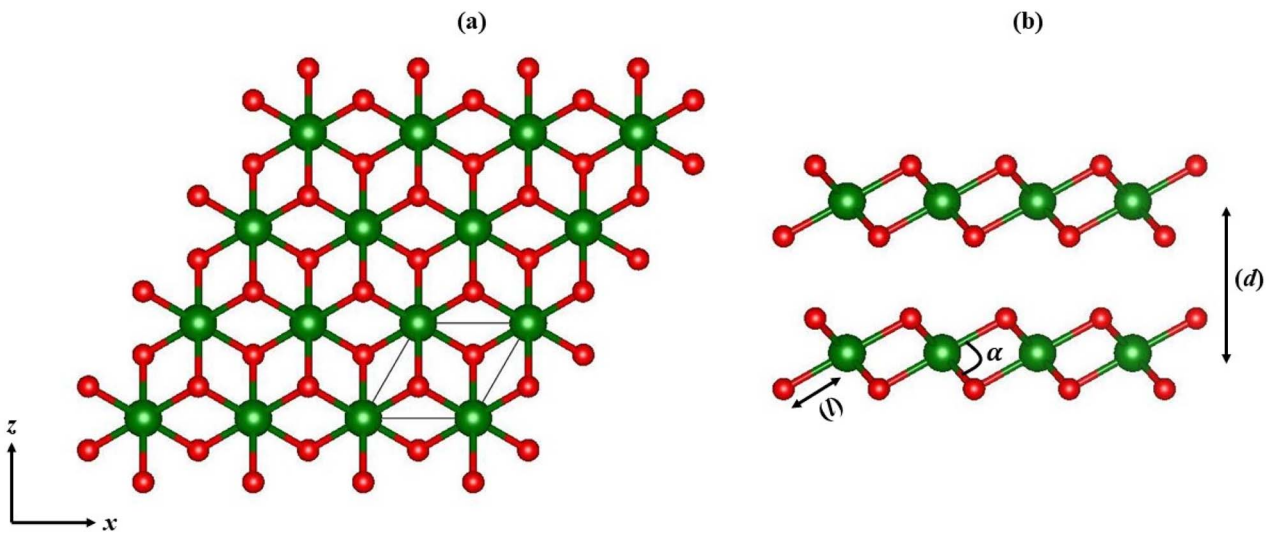

Fig. 1 Optimized crystal structure of an XO_2 bilayer with (a) top view and (b) side view. Green and red atoms represent X and O atoms, respectively.

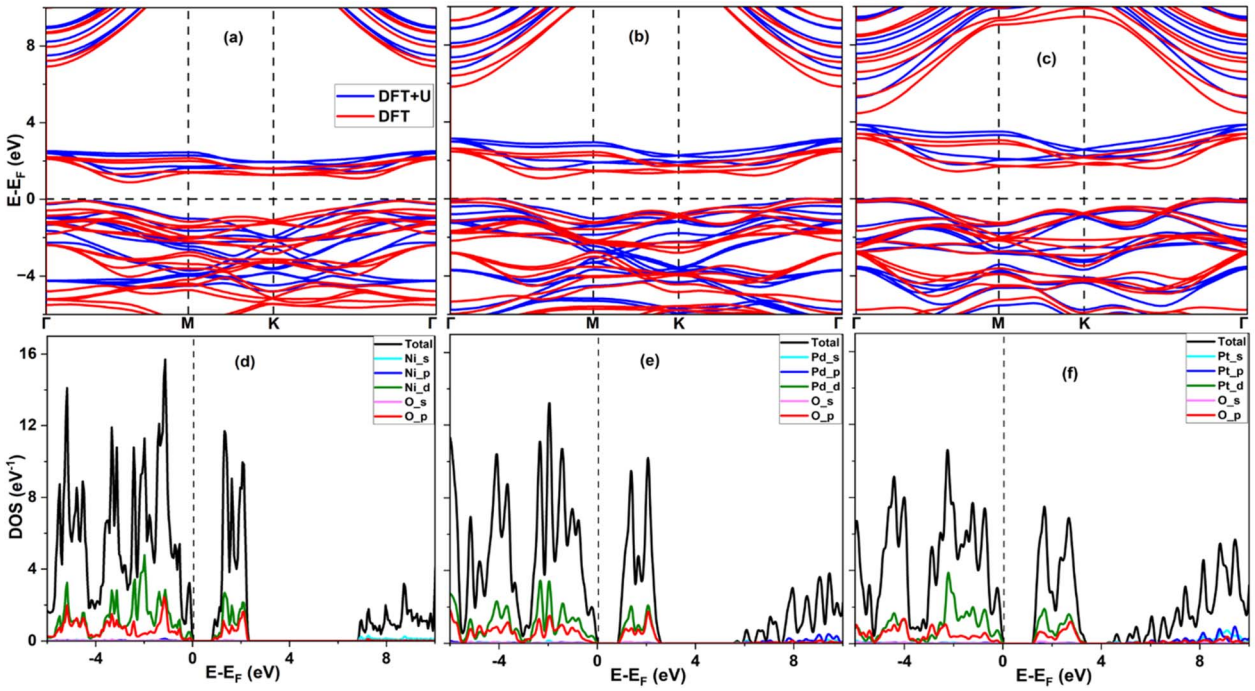

Fig. 2 Plots of the electronic band structure and density of states of (a and d) NiO_2, (b and e) PdO_2 and (c and f) PtO_2 bilayers, respectively.

counterparts. The presence of valence and conduction band extrema along the Γ–M path of the Brillouin zone indicates indirect band-gap semi-conducting nature which is similar in all monolayers and their corresponding bilayers. However, it is worth noting that the band-gap has decreased in all three bilayers. In most cases, it is observed that bilayers exhibit a reduction in the band-gap when compared to their monolayer counterparts. This phenomenon can be attributed to intrinsic strains, which lead to an increase in lattice parameters and, consequently, inter-atomic spacings. This effect is primarily driven by the van der Waals interactions between the layers. The magnitude of the band-gap is found to vary inversely with atomic spacing which clarifies our results. The separation between two maxima of valence bands along the Γ–M and Γ–K paths is zero, indicating complete degeneracy. In contrast, the two minima of conduction bands along the same paths are separated by 0.18 eV, 0.14 eV, and 0.12 eV in the case of NiO_2, PdO_2 and PtO_2 bilayers, respectively. This demonstrates that the conduction band minima are partially degenerate. The degeneracy of bands near the Fermi level plays a significant role in influencing both the Seebeck coefficient and electrical conductivity. This type of degeneracy, when present, leads to simultaneous enhancement of both these parameters, which is highly advantageous for the thermoelectric performance of a material.

The conventional DFT methods underestimate the electronic band-gap of highly correlated systems (d/f-block elements) due to over-delocalization of valence electrons. Due to the presence of d-block elements (X atoms) in XO_2 bilayers, DFT + *U* Hubbard correction needs to be incorporated to get a precise value of the electronic band-gap. The Hubbard correction has the effect of widening the band-gap in the bilayers, which is depicted in Fig. 2 and detailed in Table 1. As a result of the *U* correction, there is no alteration in the dispersion of the band extremum, but there is a slight upward shift in the position of conduction band maxima. This can be attributed to the predominant contribution of d-orbitals of X atoms in the conduction band formation near the Fermi level. The reflection of the band structure in the form of partial and total density of states (DOS) is presented in Fig. 2. The XO_2 bilayers feature larger peak magnitudes of DOS close to the Fermi level. This leads to a highly asymmetric DOS near band edges. This characteristic is advantageous as it contributes to the enhancement of thermoelectric performance due to the asymmetry in charge carrier transportation from the hot side to the cold side and *vice versa*. The valence band and conduction band states near the Fermi level are the result of hybridization between d-orbitals of X atoms and p-orbitals of O atoms. The presence of transition-metal elements (X; from the d-block) with valence electrons occupying both s and d-orbitals, along with chalcogen elements (O; from the p-block) with valence electrons found in s and p-orbitals, results in a type of hybridization between orbitals known as "mixed s–d and s–p hybridization". The sharp peaks in the DOS result from the interplay of band degeneracy and flatness of bands near the Fermi level.

Relaxation time and carrier mobility

In constant relaxation time approximation (CRT), adopted by the BoltzTrap code for transport property calculations, a fixed value of 10^{-14} s is utilized as the relaxation time ($\tau(0)$) for all materials, irrespective of their properties and temperature.[47] Nevertheless, it is crucial to emphasize that the precise value of

the relaxation time $\tau(T)$ is temperature dependent and may differ from one material to another, contingent on their specific physical characteristics. The value of $\tau(T)$ is determined by the quantity and nature of charge carrier scattering events within the material. Various sources of scattering can impact $\tau(T)$, but the predominant mechanism is the interaction of charge carriers with thermal phonons, which hinders the flow of charges and consequently reduces $\tau(T)$. The widely accepted deformation potential theory for thermoelectric transport calculations, developed by Bardeen and Shockley, can be used to explain this type of interaction. According to this theory, $\tau(T)$ can be written as:[48]

$$\tau(T) = \frac{m^*\mu}{e} \quad (3)$$

Here m^* is the effective mass of the carrier which is computed from the electronic band structure using $m^* = \frac{\hbar^2}{\partial^2 E/\partial k^2}$, where $\hbar$ is the reduced Planck constant and $\partial^2 E/\partial k^2$ is the second order derivative of the band energy (E) with respect to the wave vector (k) along the Γ–M path of the irreducible Brillouin zone.[49] The μ represents the ease of flow of charges called mobility defined as:

$$\mu = \frac{e\hbar^3\, C_\beta{}^{2D}}{k_B\, Tm^* m_d^* \left(E_\beta^*\right)^2} \quad (4)$$

where electronic charge, Boltzmann constant and temperature are identified as e, k_B and T, respectively.[50] $C_\beta{}^{2D}$ is a two-dimensional elastic constant which is obtained by parabolic fitting of the total energy with strain, given as $C_\beta{}^{2D} = \frac{\partial^2 E}{A\partial(s)^2}$ and E_β^* is the deformation potential constant which is calculated by linear fitting of shift in the valence/conduction band edge with strain, given as $E_\beta^* = \frac{\Delta E_{(Edge)}}{\Delta s}$.[51] Also, $s = \Delta l/l_o$ is the applied fractional strain with $\Delta l = (l - l_o)$ and l_o is the equilibrium lattice constant. The values obtained for all of these parameters are presented in Table 2. The calculated electron and hole mobilities for the XO_2 (X = Ni, Pd, Pt) bilayers are indeed relatively low compared to conventional 2D semiconductors. This behavior can be attributed primarily to the low dispersion of both the conduction and valence bands in these systems, as observed in our calculated band structures. The resulting large effective masses of charge carriers significantly reduce their mobility, as described by the deformation potential theory. In addition, low carrier mobility is a well-known characteristic of many transition metal oxides, especially those containing partially filled d-orbitals. The presence of localized d states leads to reduced carrier delocalization, and often enhances electron–phonon coupling, which further limits mobility. Experimental and theoretical studies on oxide semiconductors such as NiO, TiO_2, and $SrTiO_3$ also report relatively low mobilities, often in the range of 1–10 $cm^2\ V^{-1}\ s^{-1}$ or lower under ambient conditions. This behaviour is consistent with our findings and reinforces the notion that the low mobilities observed are an intrinsic feature of these materials. However, it is important to note that the higher density-of-states effective mass in these oxides contributes to an enhanced Seebeck coefficient, which partially compensates for the low mobility and leads to an overall improvement in the power factor. This trade-off is characteristic of many oxide-based thermoelectrics and aligns well with the trends observed in our study. The increase in carrier effective mass from the monolayer to bilayer structure results in a decrease in overall mobility. This observation aligns with the common trend seen in 2D materials, where the mobility tends to decrease with an increase in the number of layers, consistent with the general rule governing layer-dependent effective mass.[52,53] The calculated values of different parameters suggest that interlayer coupling yields a mean impact on both E_β^* and $\tau(T)$, when compared with intrinsic monolayers. This demonstrates that bilayer engineering introduces a synergistic effect, akin to a "cocktail" of factors, resulting in a relatively increased $\tau(T)$. This robust principle holds promise as a potential approach to control the electron–phonon interaction in 2D thermoelectric materials. Additionally, it is noteworthy to observe an enhanced elastic modulus in bilayers, indicating improved mechanical properties compared to their intrinsic monolayers.

Lattice dynamics and thermal conductivity

Lattice dynamics has a crucial effect on thermoelectric performance of a material. Mostly, the phonon dispersion is used to analyse the thermal behaviour of a material and is a good measure of dynamic stability. The phonon spectra of AA stacked XO_2 bilayers along high symmetry paths are shown in Fig. 3. The

Table 2 Calculated values of the elastic constant ($C_\beta{}^{2D}$), deformation potential constant (E_β^*), effective mass (m^*), mobility (μ at 300 K) and relaxation time (τ at different temperatures) of XO_2 bilayers

						$\tau \times 10^{-14}$ (s)		
Material	Carrier type	$C_\beta{}^{2D}$ (Nm^{-1})	E_β^* (eV)	m^* (m_e)	μ ($cm^2\ V^{-1}\ s^{-1}$)	300 K	500 K	700 K
NiO_2	e	147.06	−16.50	1.35	6.32	4.92	2.87	2.50
	h	147.06	−11.81	2.34	4.07	5.53	3.36	2.36
PdO_2	e	101.26	−20.83	1.40	2.54	2.05	2.18	1.43
	h	101.26	−15.60	3.68	0.67	2.33	1.74	1.61
PtO_2	e	117.37	−26.33	1.49	1.63	1.34	1.08	0.74
	h	117.37	−18.79	1.95	1.88	2.86	1.92	1.66

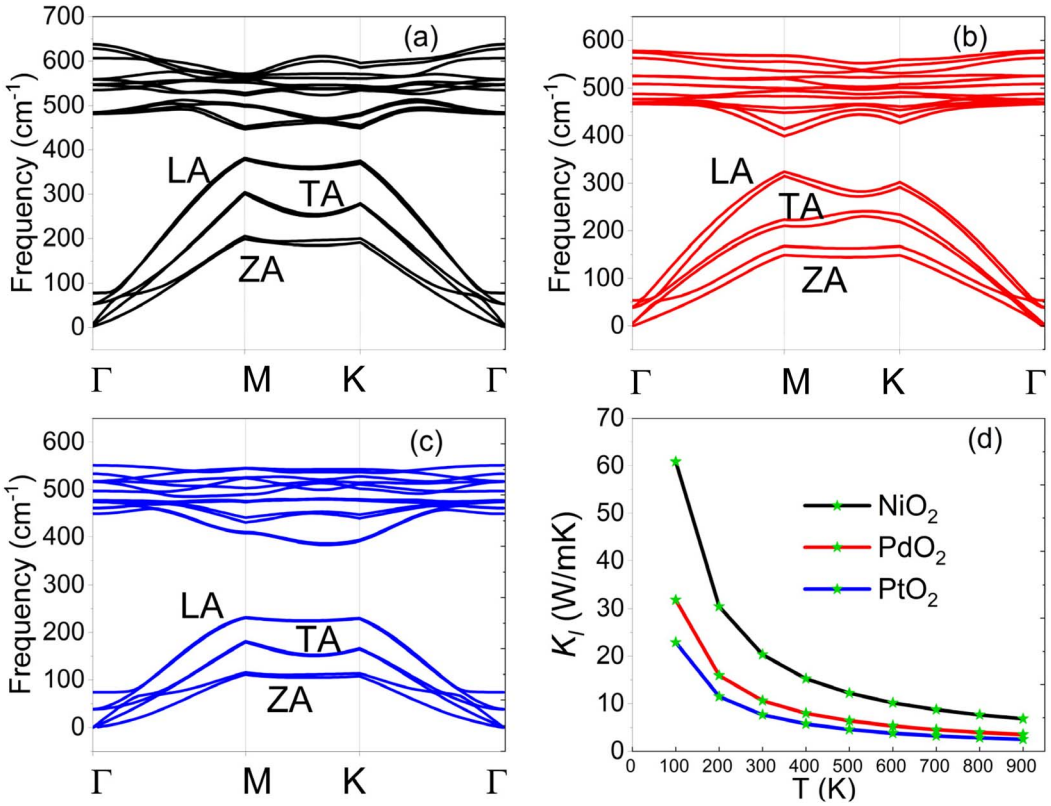

Fig. 3 Plots depicting phonon band structures (a–c) and lattice thermal conductivity (d) of XO_2 bilayers at various temperatures.

phonon band structure, showcasing all vibrational modes within the positive frequency range, confirms the dynamic stability of AA stacked XO_2 bilayers. Three acoustic and fifteen optical branches are generated by the vibration of six atoms in the primitive unit cell of the bilayers. The number of phonon branches in bilayers is twice that of their monolayer structures, primarily because of doubling of atoms in the unit cells. The presence of optical branches in the frequency range of 35–95 cm^{-1} reflects the presence of weak interlayer interaction between two XO_2 monolayers. Similar type of behaviour is found in some other bilayers like SnSe,[29] SnTe[30] and GeSe.[25] The higher group velocity observed in acoustic phonon modes compared to optical modes results in acoustic phonons predominantly carrying the thermal current, while optical phonons contribute only minimally.[54] Hence, lattice thermal conductivity primarily depends on characteristics of acoustic phonon branches. The lowest frequency out-of-plane flexure optical (ZO) branches anticross the acoustic branches close to the Γ point in all three cases. This in turn will promote the energy–momentum conservation selection rules and enhance the scattering rate of acoustic phonons, consequently decreasing their lifetime. Meanwhile, the softening of acoustic branches will further bring anharmonicity in the crystal and reduce phonon group velocity. As a result, the three phonon inelastic scattering rates will be improved along with a diminished phonon flow, resulting in a reduction in lattice thermal conductivity (κ_l). As the atomic mass increases from Ni to Pd and then to Pt, the frequencies of the acoustic phonon branches systematically shift to lower values. This trend arises from the inverse relationship between atomic mass and phonon frequency, resulting in NiO_2 exhibiting the highest acoustic branch frequencies, while PtO_2 shows the lowest. To gain deeper insight into the lattice dynamics, we have computed the atom-projected phonon density of states (PDOS), as shown in the SI (Fig. S1 (a–c)). The results reveal that the low-frequency phonon modes are predominantly contributed by the heavier transition metal (X = Ni, Pd, Pt) atoms, whereas the high-frequency modes are largely governed by the lighter oxygen atoms. This separation of vibrational contributions is typical in transition metal oxides and has important implications for thermal transport, as the low-frequency modes, associated with the X atoms, play a key role in carrying heat and are more susceptible to phonon scattering. Additionally, the out-of-plane acoustic (ZA) branch softens at higher atomic masses. The softening of these modes indicates the presence of weak interatomic bonding and the likelihood of strong anharmonicity. These ZA branches make a greater contribution towards lattice thermal conductivity because of their quadratic dispersion, even though they possess lower phonon group velocity. This will further affect the flow of heat current through the materials. Based on the discussion, it can be concluded that the lattice thermal conductivity of XO_2 bilayers will indeed be lower than that of their monolayer counterparts. Furthermore, the lattice thermal conductivity is expected to follow the order $PtO_2 < PdO_2 < NiO_2$. In practical applications involving 2D materials, the out-of-plane vibrations associated with the ZA modes are significantly damped when

the material is placed on a substrate. As a result, κ_l will further be significantly reduced. The same effect is observed for 2D graphene, where κ_l is reduced from ~3000 W m^{-1} K^{-1} for suspended graphene[55] to ~600 W m^{-1} K^{-1} for substrate supported graphene[56] at room temperature. In the following section, we investigate the κ_l of XO_2 bilayers to support this conclusion.

We calculate the lattice thermal conductivity by solving the Boltzmann transport equation (BTE).[42] According to BTE theory, the lattice thermal conductivity tensor κ_l for the α, β component is determined from the following summation:

$$\kappa_l, \alpha\beta = \sum_{q\lambda} c_v \, v_g^{\alpha}(q,\lambda) v_g^{\beta}(q,\lambda) \tau(q,\lambda) \quad (5)$$

where summation is over all phonon modes with wave vector q and branch index λ, and v is the phonon group velocity. c_v and $\tau(q,\lambda)$ are specific heat of a material and phonon relaxation time, respectively. The convergence of lattice thermal conductivity with respect to q-grid, cutoff distance and number of nearest neighbors is carried out. The plots are shown in Fig. S2 of the SI. The parameter $\tau(q,\lambda)$ is directly linked to the Grüneisen parameter (γ), which measures the level of anharmonicity and consequently the thermal resistance of a material. The variation of κ_l of XO_2 bilayers at different temperatures is presented in Fig. 3(d). The value of κ_l for NiO_2, PdO_2 and PtO_2 bilayers at room temperature is 23.91 W m^{-1} K^{-1}, 12.18 W m^{-1} K^{-1} and 4.84 W m^{-1} K^{-1}, respectively. These values are considerably lower when compared to their monolayer counterparts (51.77 W m^{-1} K^{-1}, 15.85 W m^{-1} K^{-1} and 12.41 W m^{-1} K^{-1}, respectively). Fig. S3 shows the Grüneisen parameter (γ) and phonon group velocity of XO_2 monolayers at room temperature. The plots indicate that XO_2 monolayers exhibit lower γ than the bilayers, suggesting that bilayers have stronger anharmonicity, which typically leads to lower thermal conductivity. Furthermore, because of softening of the phonon mode, phonon group velocity in bilayers is lower than in monolayer counterparts, further supporting the trend of reduced thermal conductivity in bilayers. The contribution of various atoms to γ and its relationship with phonon frequency are depicted in Fig. 4(a–c). It is evident from the figure that both X and O atoms contribute almost equally to phonon scattering across all bilayers. However, the magnitude of γ decreases as the mass of X increases, progressing from NiO_2 to PdO_2 and to PtO_2. This trend can be attributed to the opening of the bandgap between acoustic branches and low-frequency optical branches, which suppresses three-phonon scattering channels in accordance with the selection rules. This suppression reduces anharmonicity and consequently, γ, which in turn leads to longer mean free path of phonons and higher κ_l. Hence, based on this discussion, one would expect the κ_l to increase from NiO_2 to PtO_2. However, contrary to this expectation, a reverse trend is observed. To elucidate this anomalous behaviour, the influence of phonon group velocity (v_g) on κ_l is analysed and illustrated in Fig. 4(d–f). The v_g quantifies the rate of thermal energy flow and is directly associated with κ_l. The decline in v_g of the bilayers from NiO_2 to PtO_2 is evident from Fig. 4(d–f). This decrease in v_g occurs due to the softening of phonon modes with an increase in atomic mass. Such a decrease adversely affects κ_l and justifies its declining trend (PtO_2 < PdO_2 < NiO_2) observed in XO_2 bilayers. With an increase in temperature, the value of κ_l falls because of the rise in inelastic phonon scattering. At 700 K, κ_l drops to 8.69 W m^{-1} K^{-1}, 4.71 W m^{-1} K^{-1} and 1.93 W m^{-1} K^{-1}, respectively, for NiO_2, PdO_2 and PtO_2 bilayers. With reduced κ_l in XO_2 bilayers in contrast to their monolayer counterparts, improved efficiency can be anticipated through bilayer engineering.

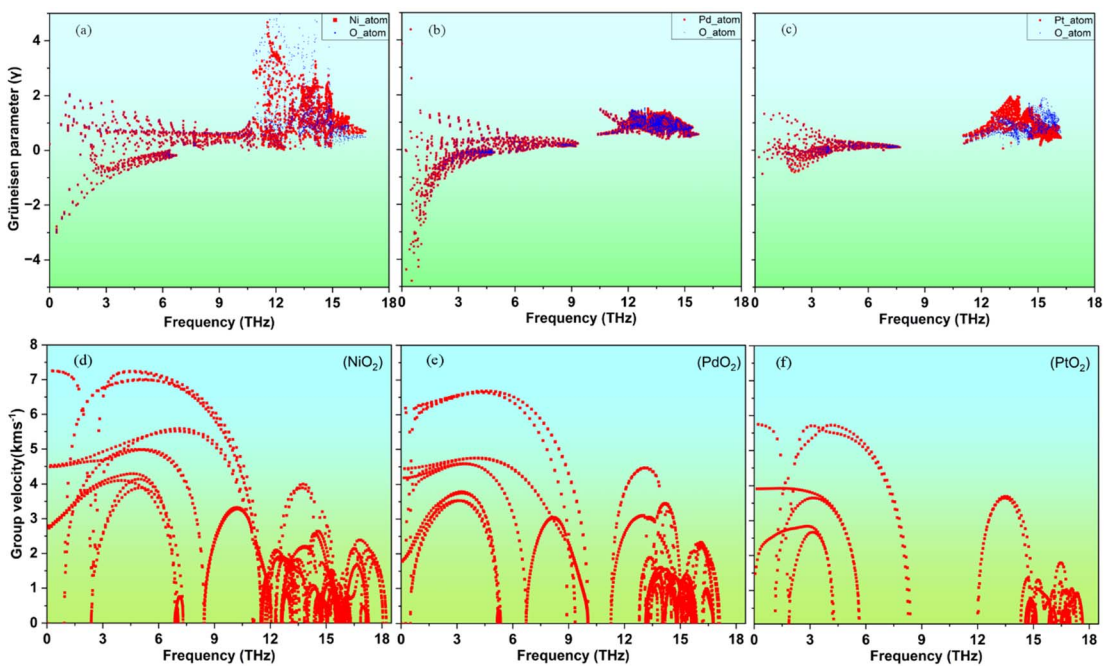

Fig. 4 Variation of the (a–c) Grüneisen parameter (γ) and (d–f) group velocity (v_g) with frequency for NiO_2, PdO_2 and PtO_2 bilayers, respectively.

Table 3 Electronic transport parameters of NiO_2, PdO_2 and PtO_2 bilayers and their figure of merit (ZT)

Material	Temperature (K)	S (μ VK^{-1})	σ (S m^{-1}) $\times 10^6$	k_l (Wm^{-1} K^{-1})	ZT
NiO_2	300	1560	7.85	20.29	0.57
	500	936	4.65	12.18	0.69
	700	670	3.21	8.69	1.05
PdO_2	300	1985	5.47	10.60	0.37
	500	1196	4.19	6.36	1.12
	700	848	2.59	4.54	1.57
PtO_2	300	2281	4.29	7.62	0.53
	500	1356	2.86	4.57	0.99
	700	958	2.20	3.26	1.79

Transport parameters

In this section, we have simulated the transport parameters of NiO_2, PdO_2 and PtO_2 bilayers, and listed in Table 3. The Seebeck coefficient (S), which is a measure of voltage developed across a material, when subjected to a temperature gradient, is calculated using the expression:

$$S(\mu, T) = \frac{ek_B}{\sigma}\int d\varepsilon\left(-\frac{\partial f_\mu(\varepsilon, T)}{\partial \varepsilon}\right)\Xi(\varepsilon)\frac{\varepsilon-\mu}{k_B T} \quad (6)$$

where $\Xi(\varepsilon)$ and $f_\mu(\varepsilon,T)$ are the transport function and distribution function, respectively, ε is the energy and μ is the electrochemical potential.[57] Due to the broadening of function $\partial f/\partial\varepsilon$ with energy, it is adequate to consider only a small energy range around $\mu = 0$ rather than the entire energy spectrum when calculating transport coefficients.[58] Therefore, we focused exclusively on the energy range of -1.5 eV $< \mu <$ 1.5 eV. The behavior of S with respect to μ at different temperatures is shown in Fig. S4 (top panel). The S varies abruptly near $\mu = 0$ due to the Dirac delta nature of the term $\partial f/\partial\varepsilon$ present in eqn (6). Furthermore, near $\mu = 0$, the density of states changes discontinuously which changes the sign of S. The peak value of S for NiO_2, PdO_2 and PtO_2 bilayers is 1560 (1512) μV K^{-1}, 1985 (1864) μV K^{-1} and 2281 (2242) μV K^{-1}, respectively, for electron (hole) doping at 300 K. The high value of S can be attributed to the sharp and elevated peaks in DOS near the Fermi level. Moreover, the flattening of the band extremum results in an increase in band effective mass, subsequently leading to a high value of S. Both the top of the valence band and bottom of the conduction band exhibit degeneracy along the Γ–M and K–Γ paths, as evident from the electronic band structure. This degeneracy contributes to an increased density of states effective mass of carriers, consequently boosting S, since they are directly linked as per the Mott equation.[58] The calculated values of S for XO_2 bilayers are lower than their monolayer counterparts at all temperatures. This fall in S is ascribed to the closing of the band-gap of bilayers, which increases the bipolar conduction effect. Additionally, the PtO_2 bilayer possesses the highest band-gap, followed by PdO_2, and then NiO_2. This same order is also observed in S, with PtO_2 having the highest S value, followed by PdO_2, and then NiO_2. Besides, XO_2 bilayers have higher values of S compared to the following bilayers: SnSe ($\sim$450 μV K^{-1}),[29] SnTe ($\sim$400 μV K^{-1})[30] and GeSe ($\sim$950 μV K^{-1}),[25] XI_2 {X = Ge, Sn, Pb} ($\sim$600 μV K^{-1}),[27] monolayers; SnP_3 (907 μV K^{-1}),[20] Be_3X_2 {X = C, Si, Ge, Sn} ($\sim$50–100 μV K^{-1})[59] and some transition metal oxides.[24]

Fig. S4 (middle panel) illustrates the electrical conductivity (σ) and electronic component of the total thermal conductivity (κ_e) of XO_2 bilayers. The precise values of σ are obtained using the temperature dependent τ, as calculated above. The trend followed by σ is opposite to that of S. This is mainly due to the strong dependence of σ on the band gap. Consequently, at room temperature, NiO_2 (7.85 (5.39) $\times$ 10^6 S m^{-1}) exhibits higher conductivity than PdO_2 (5.47 (3.58) $\times$ 10^6 S m^{-1}), followed by PtO_2 (4.29 (2.80) $\times$ 10^6 S m^{-1}) for hole (electron) doping. The higher σ value for electron doping compared to hole doping is related to $\tau(T)$, which is greater for holes than for electrons in all three bilayers. The drop in σ with increasing temperature is primarily a consequence of the increased scattering of electrons by phonons. There is approximately a tenfold increase of σ in XO_2 bilayers as compared to their monolayer counterparts. This notable improvement is attributed to the simultaneous reduction in the bandgap and an increase in $\tau(T)$. Additionally, the magnitude of DOS near the Fermi level is enhanced (due to the degeneracy of the band extremum) in all three bilayers resulting in an elevation of σ. Fig. S4 (bottom panel) illustrates the behavior of κ_e against μ at various temperatures. The trend exhibited by κ_e with respect to temperature aligns with that of σ because they are linked through the Wiedemann–Franz law (κ_e

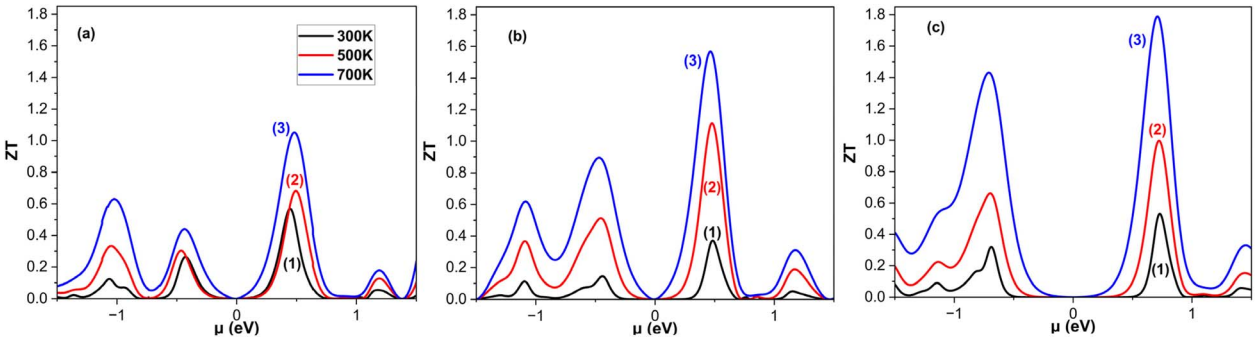

Fig. 5 Figure of merit (ZT) of (a) NiO_2 (b) PdO_2 and (c) PtO_2 bilayers as a function of chemical potential at various temperatures.

$= \sigma LT$).[55] Here, L stands for the Lorenz number whose value for non-degenerate semiconductors is 1.5×10^{-8} W S^{-1} K^{-2}. The trend followed by κ_e in bilayers is $PtO_2 < PdO_2 < NiO_2$ and is higher than their corresponding monolayers because of obvious reasons.

The figure of merit (ZT), which quantifies the thermoelectric performance of a material, is calculated at various temperatures as a function of μ and is depicted in Fig. 5. Due to the opposite behavior of S and σ with μ, ZT first increases and then decreases on both sides, close to $\mu = 0$. Even though σ is lower for the PtO_2 bilayer, it exhibits a higher value of S and lower κ_l compared to other two bilayers. Consequently, PtO_2 has the highest value of ZT among the three. The maximum values of ZT for NiO_2, PdO_2 and PtO_2 bilayers, respectively, are 1.05 (0.63), 1.57 (0.89) and 1.79 (1.43). These values are obtained for electron (hole) doping at 700 K and are nearly two times higher compared to their monolayer counterparts. In practical applications, achieving the optimal Fermi level shift required for maximizing ZT is typically realized through doping. The dependence of ZT on carrier concentration is illustrated in Fig. S5. The carrier concentrations corresponding to the peak ZT values for NiO_2, PdO_2 and PtO_2 bilayers are approximately 9.3 (6.8) $\times 10^{18}$ cm^{-3}, 4.2 (4.1) $\times 10^{19}$ cm^{-3}, 4.4 (4.3) $\times 10^{19}$ cm^{-3}, respectively, for electron (hole)-doping at 700 K.

Conclusion

The impact of stacking two XO_2 monolayers to create a homobilayer on thermoelectric performance is examined in the current work utilizing density functional theory and Boltzmann transport equations. The chemical and dynamic stability of XO_2 bilayers, with AA stacked configuration, is validated based on binding energy and phonon dispersion calculations. Using the conventional DFT method, band gaps of 0.89 eV, 1.0 eV and 1.43 eV are obtained for NiO_2, PdO_2 and PtO_2 bilayers, respectively. On implementing Hubbard U correction (DFT + U), the band gaps open up to 1.18 eV, 1.53 eV and 1.79 eV, respectively These values are lower than those of their pristine monolayers, showcasing the dependency of the electronic band structure on the interlayer interactions. Near about two times reduction in lattice thermal conductivity is found in XO_2 bilayers compared to their monolayer structures, which is justified by softening of phonon modes, reduced phonon group velocity, overlap between acoustic and optical branches, and high Grüneisen parameter. Although the Seebeck coefficient is lower compared to their monolayer counterparts, due to the reduction in the band gap, the electrical conductivity increases by nearly ten times which results in an overall increase in power factor. The combined effect of fall in lattice thermal conductivity and rise in power factor leads to a ZT of 1.05 (0.63), 1.57 (0.89) and 1.78 (1.43) for NiO_2, PdO_2 and PtO_2 bilayers, respectively, for electron (hole) doping at 700 K. These values are near about two times higher than their pristine monolayers. Since XO_2 bilayers have a higher thermoelectric response compared to their monolayer counterparts, our research demonstrates that the inter-layer contact is crucial to thermoelectric performance of a material. It offers a practical means of adjusting the thermoelectric properties and will be very useful in subsequent experimental research.

Conflicts of interest

There are no conflicts to declare.

Data availability

Data will be made available on request.

Supplementary information is available: Atom-projected phonon density of states (PDOS), harmonic force constants for the nearest-neighbor atom pairs for XO_2 bilayers along a and z-directions. Convergence of lattice thermal conductivity with respect to q-grid, cutoff distance and nearest neighbors. Grüneisen parameter and group velocity. Transport parameters and figure of merit (ZT) as a function of chemical potential at different temperatures. See DOI: **https://doi.org/10.1039/d5na00303b**.

References

1 M. Aneke and M. Wang, *Appl. Energy*, 2016, **179**, 350–377.
2 M. A. Karri, E. F. Thacher and B. T. Helenbrook, *Energy Convers. Manag.*, 2011, **52**, 1596–1611.
3 Z. H. Dughaish, *Phys. B Condens. Matter*, 2002, **322**, 205–223.
4 J. Yang, L. Xi, W. Qiu, L. Wu, X. Shi, L. Chen, J. Yang, W. Zhang, C. Uher and D. J. Singh, *npj Comput. Mater.*, 2016, **2**, 15015–15031.
5 Z. Chen, X. Zhang and Y. Pei, *Adv. Mater.*, 2018, **30**, 1658–1663.
6 W. Kim, *J. Mater. Chem. C*, 2015, **3**, 10336–10348.
7 Y. Xue, C. Gao, L. Liang, X. Wang and G. Chen, *J. Mater. Chem. A*, 2018, **6**, 22381–22390.
8 D. K. B. U. Sandhya Shenoy and H. Bantawal, *J. Phys. Chem.*, 2018, **122**, 27567–27574.
9 D. K. Bhat, H. Bantawal and U. S. Shenoy, *Nanoscale Adv.*, 2020, **2**, 5688–5698.
10 A. K. Geim, *Science*, 2009, **324**(5934), 1530–1534.
11 K. S. Novoselov, V. I. Fal'Ko, L. Colombo, P. R. Gellert, M. G. Schwab and K. Kim, *Nature*, 2012, **490**, 192–200.
12 Y. Xu, B. Yan, H. J. Zhang, J. Wang, G. Xu, P. Tang, W. Duan and S. C. Zhang, *Phys. Rev. Lett.*, 2013, **111**, 1–5.
13 A. Luican-Mayer and E. Y. Andrei, Probing Dirac Fermions in Graphene by Scanning Tunneling, Microscopy and Spectroscopy, *Physics of Graphene*, 2014, **https://www.physics.rutgers.edu/~eandrei/DF-13.pdf**.
14 Y. Xu, Z. Gan and S. C. Zhang, *Phys. Rev. Lett.*, 2014, **112**, 1–5.
15 F. Matusalem, M. Marques, L. K. Teles and F. Bechstedt, *Phys. Rev. B: Condens. Matter Mater. Phys.*, 2015, **92**, 1–8.
16 K. Watanabe, T. Taniguchi and H. Kanda, *Nat. Mater.*, 2004, **36**(3), 404–409.
17 K. S. Novoselov, *et al*, *Science*, 2016, **306**, 666–669.
18 K. F. Hsu, S. Loo, F. Guo, W. Chen, J. S. Dyck, C. Uher, T. Hogan, E. K. Polychroniadis and M. G. Kanatzidis, *Science*, 2004, **303**, 818–822.

19 W. Liu, X. Tan, K. Yin, H. Liu, X. Tang, J. Shi, Q. Zhang and C. Uher, *Phys. Rev. Lett.*, 2012, **108**, 166601–166605.
20 X. L. Zhu, P. F. Liu, J. Zhang, P. Zhang, W. X. Zhou, G. Xie and B. T. Wang, *Nanoscale*, 2019, **11**, 19923–19932.
21 T. Ouyang, E. Jiang, C. Tang, J. Li, C. He and J. Zhong, *J. Mater. Chem. A*, 2018, **6**, 21532–21541.
22 A. F. Wani, B. Rani, S. Dhiman, U. B. Sharopov and K. Kaur, *Int. J. Energy Res.*, 2022, **46**, 10885–10893.
23 S. S. Naghavi, J. He, Y. Xia and C. Wolverton, *Chem. Mater.*, 2018, **30**, 5639–5647.
24 S. Walia, S. Balendhran, H. Nili, S. Zhuiykov, G. Rosengarten, Q. H. Wang, M. Bhaskaran, S. Sriram, M. S. Strano and K. Kalantar-zadeh, *Prog. Mater. Sci.*, 2013, **58**, 1443–1489.
25 Z. Tang, X. Wang, J. Li, C. He, M. Chen, X. Li, C. Tang and T. Ouyang, *Appl. Phys. Lett.*, 2023, **123**, 102201–102208.
26 Z. Tang, X. Wang, J. Li, C. He, M. Chen, C. Tang and T. Ouyang, *Phys. Rev. B*, 2023, **108**, 214304–214316.
27 Z. Tang, X. Wang, C. He, J. Li, M. Chen, C. Tang and T. Ouyang, *Phys. Rev. B*, 2024, **110**, 134320–134330.
28 Q. Fan, F. Li, H. Wang, R. Huang, W. Chen and H. Zhang, *Adv. Funct. Mater.*, 2022, 2200516.
29 A. Pandit, *J. Mater. Sci.*, 2021, **56**, 10424–10437.
30 H. A. H. Mohammed, G. M. Dongho-Nguimdo and D. P. Joubert, *Mater. Today Commun.*, 2019, **21**, 10066.
31 Z. Li, W. Guo, T. T. Zhang, J. H. Song, T. Y. Gao, Z. B. Gu and Y. F. Nie, *APL Mater.*, 2020, **8**, 91112.
32 T. Obermüller, N. Doudin, D. Kuhness, S. Surnev and F. P. Netzer, *J. Mater. Res.*, 2017, **32**, 3924–3935.
33 J. Sun, M. R. Barone, C. S. Chang, M. E. Holtz, H. Paik, J. Schubert, D. A. Muller and D. G. Schlom, *APL Mater.*, 2019, **7**, 121112.
34 M. Brahlek, G. Rimal, J. M. Ok, D. Mukherjee, A. R. Mazza, Q. Lu, H. N. Lee, T. Z. Ward, R. R. Unocic, G. Eres and S. Oh, *Phys. Rev. Mater.*, 2019, **3**, 093401.
35 F. Sedona, G. A. Rizzi, S. Agnoli, F. X. Llabrés i Xamena, A. Papageorgiou, D. Ostermann, M. Sambi, P. Finetti, K. Schierbaum and G. Granozzi, *J. Phys. Chem. B*, 2005, **109**, 24411–24426.
36 A. F. Wani, B. Rani, S. Dhiman, U. B. Sharopov and K. Kaur, *Int. J. Energy Res.*, 2022, **46**, 8527–8535.
37 A. F. Wani, L. Patra, M. Srinivasan, J. Singh, S. A. M. Abdelmohsen, M. M. Alanazi, S. Dhiman and K. Kaur, *Adv. Theor. Simul.*, 2023, **6**, 2300158.
38 P. Giannozzi, S. Baroni, N. Bonini, M. Calandra, R. Car, C. Cavazzoni, D. Ceresoli, G. L. Chiarotti, M. Cococcioni, I. Dabo, A. Dal Corso, S. De Gironcoli, S. Fabris, G. Fratesi, R. Gebauer, U. Gerstmann, C. Gougoussis, A. Kokalj, M. Lazzeri, L. Martin-Samos, N. Marzari, F. Mauri, R. Mazzarello, S. Paolini, A. Pasquarello, L. Paulatto, C. Sbraccia, S. Scandolo, G. Sclauzero, A. P. Seitsonen, A. Smogunov, P. Umari and R. M. Wentzcovitch, *J. Phys. Condens. Matter*, 2009, **21**, 395502–395511.
39 J. P. Perdew, K. Burke and M. Ernzerhof, *Phys. Rev. Lett.*, 1996, **77**, 3865–3868.
40 J. D. Pack and H. J. Monkhorst, *J. Chem. Inf. Model.*, 1977, **16**, 1748–1749.
41 J. H. Jung, C. H. Park and J. Ihm, *Nano Lett.*, 2018, **18**, 2759–2765.
42 G. K. H. Madsen and D. J. Singh, *Comput. Phys. Commun.*, 2006, **175**, 67–71.
43 K. Kaur, D. Murali and B. R. K. Nanda, *J. Mater. Chem. A*, 2019, **7**, 12604–12615.
44 G. K. H. Madsen, J. Carrete and M. J. Verstraete, *Comput. Phys. Commun.*, 2018, **231**, 140–145.
45 L. Lindsay, W. Li, N. Mingo, D. A. Broido and T. L. Reinecke, *Phys. Rev. B: Condens. Matter Mater. Phys.*, 2014, **89**, 155426–155443.
46 J. M. Ziman, *Principles of the theory of solids*, 1964, **https://archive.org/details/principlesoftheo00zima**.
47 T. Feng, B. Qiu and X. Ruan, *Phys. Rev. B: Condens. Matter Mater. Phys.*, 2015, **92**, 235206–235212.
48 L. Xu, M. Yang, S. J. Wang and Y. P. Feng, *Phys. Rev. B*, 2017, **95**, 1–9.
49 C. Wang and G. Gao, *J. Phys. Condens. Matter*, 2020, **32**, 205503–205512.
50 A. F. Wani, S. A. Khandy, A. S. Verma, S. Dhiman and K. Kaur, *Sci. Rep.*, 2024, **14**, 1–15.
51 B. Rani, A. F. Wani, S. A. Khandy, U. B. Sharopov, L. Patra, K. Kaur and S. Dhiman, *Solid State Commun.*, 2022, **351**, 114796.
52 J. Zhang, X. Liu, Y. Wen, L. Shi, R. Chen, H. Liu and B. Shan, *ACS Appl. Mater. Interfaces*, 2017, **9**, 2509–2515.
53 A. Fayaz Wani, B. Rani, S. Dhiman and K. Kaur, *Adv. Mater. Process. Technol.*, 2023, **09**, 1–9.
54 A. Shafique, A. Samad and Y. H. Shin, *Phys. Chem. Chem. Phys.*, 2017, **19**, 20677–20683.
55 J. H. Seol, I. Jo, A. L. Moore, L. Lindsay, Z. H. Aitken, M. T. Pettes, X. Li, Z. Yao, R. Huang, D. Broido, N. Mingo, R. S. Ruoff and L. Shi, *Science*, 2010, **328**, 213–216.
56 B. Peng, D. Zhang, H. Zhang, H. Shao, G. Ni, Y. Zhu and H. Zhu, *Nanoscale*, 2017, **9**, 7397–7407.
57 A. F. Wani, S. A. Khandy, L. Patra, M. Srinivasan, J. Singh, A. M. Ali, I. Islam, S. Dhiman and K. Kaur, *Phys. Chem. Chem. Phys.*, 2023, **25**, 21736–21747.
58 M. Jonson and G. D. Mahan, *Phys. Rev. B: Condens. Matter Mater. Phys.*, 1980, **21**, 4223–4229.
59 L. Song, L. Zhang, Y. Guan, J. Lu, C. Yan and J. Cai, *Chin. Phys. B*, 2019, **28**, 3–7.